

Biomass-derived electrocatalytic composites for  
hydrogen evolution†

Cite this: *Energy Environ. Sci.*, 2013, **6**,  
1818

Wei-Fu Chen,<sup>\*a</sup> Shilpa Iyer,<sup>a</sup> Shweta Iyer,<sup>a</sup> Kotaro Sasaki,<sup>\*a</sup> Chiu-Hui Wang,<sup>ab</sup>  
Yimei Zhu,<sup>b</sup> James T. Muckerman<sup>\*a</sup> and Etsuko Fujita<sup>a</sup>

The production of hydrogen from water electrolysis calls for an efficient non-precious-metal catalyst to make the process economically viable because of the high cost and the limited supply of the currently used platinum catalysts. Here we present such a catalyst made from earth-abundant molybdenum and common, humble soybeans (MoSoy). This catalyst, composed of a catalytic  $\beta$ -Mo<sub>2</sub>C phase and an acid-proof  $\gamma$ -Mo<sub>2</sub>N phase, drives the hydrogen evolution reaction (HER) with low overpotentials, and is highly durable in a corrosive acidic solution over a period exceeding 500 hours. When supported on graphene sheets, the MoSoy catalyst exhibits very fast charge transfer kinetics, and its performance rivals that of noble-metal catalysts such as Pt for hydrogen production. These findings prove that the soybean (as well as other high-protein biomass) is a useful material for the generation of catalysts incorporating an abundant transition metal, thereby challenging the exclusivity of platinum catalysts in the hydrogen economy.

Received 21st February 2013  
Accepted 10th April 2013

DOI: 10.1039/c3ee40596f

www.rsc.org/ees

## Introduction

Hydrogen, the next generation energy carrier that can efficiently be used to produce electricity from its stored chemical energy, is a promising power source for vehicular and stationary applications, solving the twin problems of depletion of fossil fuel reserves and CO<sub>2</sub> emissions.<sup>1,2</sup> Sustainable and affordable hydrogen production is indispensable for the approaching commercialization of proton exchange membrane (PEM) fuel cells. The interconversion of water and hydrogen ( $2\text{H}_2\text{O}_{(l)} \rightarrow 2\text{H}_{2(g)} + \text{O}_{2(g)}$ ) by a carbon-free energy source such as solar or wind power is a sustainable energy storage approach.<sup>3,4</sup> However, efficiently carrying out the hydrogen evolution reaction (HER,  $2\text{H}^+ + 2\text{e}^- \rightarrow \text{H}_2$ ) under acidic conditions remains difficult without the use of platinum catalysts. The U. S. Department of Energy (DOE) has set a cost goal for hydrogen of \$2.00–3.00 per kg,<sup>5</sup> including production, delivery and dispensing, a level at which the DOE estimates that hydrogen will be cost competitive with petroleum fuels. According to a 2012 DOE report,<sup>6</sup> a large part of the capital cost of an industrial proton-exchange-membrane electrolyzer is the cost of the “membrane-electrode-assembly”, and half of that cost is due to

the use of platinum. The state-of-the-art hydrogen production cost is \$4–5 per kg based on Pt-catalyzed electrolysis devices. The high cost (\$1580 per oz in Jan 2013) and low availability of Pt make its use an impediment to large-scale commercial processes.

The challenge in hydrogen production is to reduce the use of noble metals<sup>7</sup> or replace them with inexpensive non-precious metal catalysts.<sup>8–10</sup> Three major strategies have been adopted for overcoming this challenge, including (i) optimization of the metal-hydrogen bond strength,<sup>11–14</sup> (ii) use of metal-coordination shells to alter electronic properties,<sup>15–19</sup> and (iii) nanostructuring the surfaces to increase the number of reactive sites.<sup>20–22</sup> Molybdenum, one of the most abundant transition metals, contributes high corrosion resistance to stainless steel but is unsatisfactory in electrocatalytic activity towards hydrogen evolution. There has therefore been an ongoing effort to find an affordable hydrogen production route based on molybdenum sulfide, not only for water electrolysis<sup>23</sup> but also for photoelectrochemical water splitting.<sup>24,25</sup> Hu *et al.* have developed a series of scalable MoS<sub>2</sub> and MoS<sub>3</sub> thin film systems.<sup>26–29</sup> Jaramillo *et al.* have expended considerable effort in nanostructuring MoS<sub>2</sub>.<sup>30–32</sup>

The focus of our current research has been to search for low-cost molybdenum catalysts with components from Nature's catalogue, and to develop simple, green and environmentally friendly synthetic routes. We sought high activity in acidic media and a more readily scalable synthetic procedure at an economical cost target. Through extensive exploratory testing of ordinarily available biomass including leaves, stems, flowers, seeds, and legumes (see Fig. S1 in the ESI†), we discovered that

<sup>a</sup>Chemistry Department, Brookhaven National Laboratory, Upton, NY 11973, USA.  
E-mail: wfchen@bnl.gov; ksasaki@bnl.gov; muckerman@bnl.gov; Tel: +1 631 344 4368

<sup>b</sup>Condensed Matter Physics & Materials Science Department, Brookhaven National Laboratory, Upton, New York 11973, USA

† Electronic supplementary information (ESI) available: Electrochemical measurements and parameters, BET surface area, Rietveld refinement, TGA thermograms, EDX spectra, SEM images, Faradaic yield and impedance spectra. See DOI: 10.1039/c3ee40596f

the combination of humble soybeans and molybdenum yielded a highly active catalyst. This finding not only provides a means to enhance the activity of non-precious-metal catalysts for acidic electrolytes but also inspires the development of biomass-derived catalysts for catalytic reactions.

## Results and discussion

### Synthesis and correlation of structures with HER performance

Here we show that active catalysts can be produced by the solid-state reaction of soybeans and ammonium molybdate ( $(\text{NH}_4)_6\text{Mo}_7\text{O}_{24} \cdot 4\text{H}_2\text{O}$ ). Ammonium molybdate was dissolved in water, followed by the addition of ground soybean powder. The mixture was ultra-sonicated, dried and calcined at  $800^\circ\text{C}$  under Ar in a tube furnace. A dark grey powder ( $\text{Mo}_x\text{Soy}$ ,  $x$ : weight ratio of the Mo precursor to soybean powder) was obtained. To evaluate the HER performance, we exposed a series of  $\text{Mo}_x\text{Soy}$  catalysts ( $x = 0.1, 0.25$ , and  $1$ ) to a  $\text{H}_2$ -saturated  $0.1\text{ M HClO}_4$  solution in a standard three-electrode electrochemical cell at room temperature. Fig. 1a reports the current densities obtained during a linear sweep voltammetry experiment of the  $\text{Mo}_x\text{Soy}$  catalysts coated on carbon paper. A reductive process is

observed as the electrochemical potential is applied below  $-0.05\text{ V}$  for the  $\text{Mo}_1\text{Soy}$  catalyst. Hydrogen bubbles evolved more vigorously on the electrode with higher  $x$  values. For comparison, experiments with a commercial Pt/C catalyst (E-TEK 20 wt% Pt/XC-72), a bulk Pt disk and a control sample (assigned as Soy which is prepared by annealing soybean powder only) were also performed. The Pt/C catalyst exhibited high HER catalytic performance with a small overpotential,  $\eta_{10}$  (defined as the potential at  $10\text{ mA cm}^{-2}$  of cathodic current density) of  $61\text{ mV}$ . We chose  $10\text{ mA cm}^{-2}$  as the point of reference because under 1 Sun of AM 1.5 illumination, the solar photon flux produces a charge-carrier flux of  $10\text{--}20\text{ mA cm}^{-2}$  to a planar electrode surface.<sup>4</sup> The voltammetry curve recorded with a bulk platinum electrode (grey dotted curve, Fig. 1a) showed an overpotential of  $137\text{ mV}$  for the HER. The slope of the current response of the bulk Pt electrode is low at higher current densities because of the covering of visible hydrogen bubbles on the surface of the Pt electrode which induces mass transport resistance. In contrast, the  $\text{Mo}_1\text{Soy}$  catalyst exhibits a  $\eta_{10}$  value of  $177\text{ mV}$  (red curve) and rivals the performance of the bulk Pt. At overpotentials higher than  $180\text{ mV}$ , the  $\text{Mo}_1\text{Soy}$  catalyst shows a further enhanced current density that

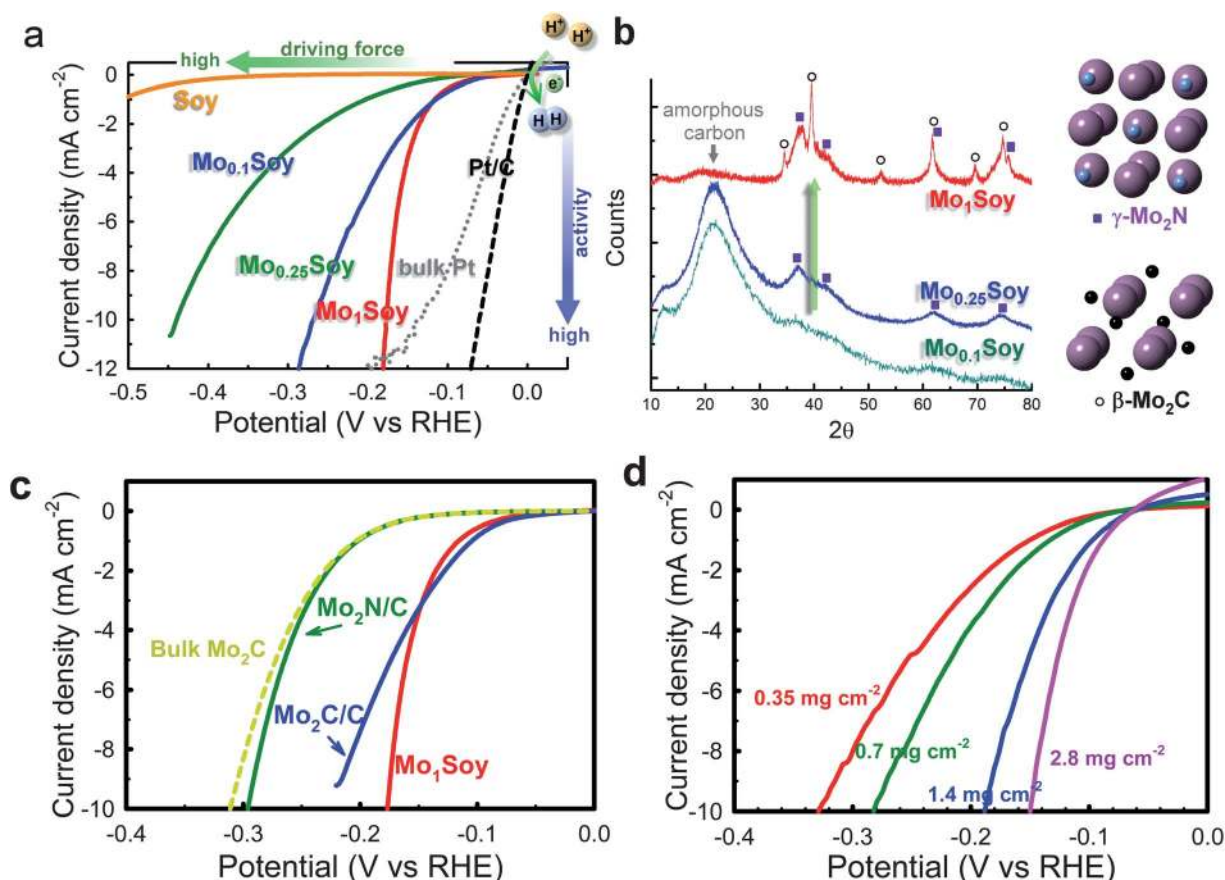


**Fig. 1** (a) The polarization curves for the hydrogen evolution reaction on  $\text{Mo}_x\text{Soy}$  catalysts, bulk Pt (grey dotted curve), and the Pt/C catalyst (black dashed curve) in  $\text{H}_2$ -purged  $0.1\text{ M HClO}_4$  solutions (scan rate  $2\text{ mV s}^{-1}$ ). The potential was referenced to the reversible hydrogen electrode. The sample made by annealing pristine soybeans is also included (orange solid line). (b) X-ray diffraction patterns corresponding to the calcined  $\text{Mo}_{0.1}\text{Soy}$ ,  $\text{Mo}_{0.25}\text{Soy}$ , and  $\text{Mo}_1\text{Soy}$  products. The assignments of the diffraction peaks are included. Schematic representation of the unit cells for  $\gamma\text{-Mo}_2\text{N}$  and  $\beta\text{-Mo}_2\text{C}$  are also shown. Plum balls: Mo, small blue balls: N, and small black balls: C. (c) The polarization curves for the HER of  $\text{Mo}_2\text{C/C}$  ( $2\text{ mg cm}^{-2}$  of  $\text{Mo}_2\text{C}$ ),  $\text{Mo}_2\text{N/C}$  ( $2\text{ mg cm}^{-2}$  of  $\text{Mo}_2\text{N}$ ), bulk  $\text{Mo}_2\text{C}$  ( $2\text{ mg cm}^{-2}$  of  $\text{Mo}_2\text{C}$ ) and the  $\text{Mo}_1\text{Soy}$  catalyst ( $1.4\text{ mg cm}^{-2}$  of  $\text{Mo}_2\text{C}$ ). (d) The polarization curves of the  $\text{Mo}_1\text{Soy}$  catalysts with different loadings of the active  $\text{Mo}_2\text{C}$  phase.

overtakes that of the bulk platinum. These voltammograms demonstrate that soybeans reduce the energy input for activating the HER on the molybdenum-incorporated electrode that has favorable proton reduction kinetics.

X-ray diffraction (XRD) was used to characterize the bulk crystal structure and average grain size of the as-synthesized  $\text{Mo}_x\text{Soy}$  catalysts. In Fig. 1b, the XRD patterns are seen to be consistent with those of tetragonal  $\gamma\text{-Mo}_2\text{N}$  (JCPDS-PDF 25-1368) and orthorhombic  $\beta\text{-Mo}_2\text{C}$  (JCPDS-PDF 77-0720) structures. It is found that the peak at  $2\theta = 22^\circ$  due to amorphous carbon is substantially reduced when the Mo content is increased, and the signals for  $\gamma\text{-Mo}_2\text{N}$  and  $\beta\text{-Mo}_2\text{C}$  phases are enhanced simultaneously. These results provide strong evidence of a solid-state reaction between the molybdate and soybeans. The grain sizes for the  $\beta\text{-Mo}_2\text{C}$  and the  $\gamma\text{-Mo}_2\text{N}$  phases in the  $\text{Mo}_1\text{Soy}$  sample calculated from the XRD data are 9.4 nm and 1.7 nm, respectively (based on the (211) peak of  $\beta\text{-Mo}_2\text{C}$  and the (111) peak of  $\gamma\text{-Mo}_2\text{N}$ ). A Rietveld refinement analysis was used to estimate the proportion of  $\text{Mo}_2\text{C}$  and  $\text{Mo}_2\text{N}$  in the  $\text{Mo}_1\text{Soy}$  catalyst. The refinement (Fig. S2 in the ESI†) shows that the weight ratio of  $\beta\text{-Mo}_2\text{C}$  to  $\gamma\text{-Mo}_2\text{N}$  is 0.55 to 0.45 in the  $\text{Mo}_1\text{Soy}$  catalyst. The content of  $\text{Mo}_2\text{C}$  crystals in the  $\text{Mo}_1\text{Soy}$  catalyst was determined by

thermogravimetric analysis (Fig. S3†) to be 17.4%. Thus, the  $\beta\text{-Mo}_2\text{C}$  and  $\gamma\text{-Mo}_2\text{N}$  loadings in the  $\text{Mo}_1\text{Soy}$  catalyst in Fig. 1a are determined to be  $1.4 \text{ mg cm}^{-2}$  and  $1.15 \text{ mg cm}^{-2}$ , respectively.

Very recently, molybdenum carbide ( $\text{Mo}_2\text{C}$ ) has been shown to be an excellent catalyst for hydrogen production.<sup>33</sup> To understand how  $\text{Mo}_2\text{C}$  and  $\text{Mo}_2\text{N}$  work in combination with each other, and how they contribute to the overall performance, we examined the isolated  $\beta\text{-Mo}_2\text{C}$  phase (carbon supported  $\beta\text{-Mo}_2\text{C}$  nanoparticles, grain size = 8.5 nm) as well as the isolated  $\gamma\text{-Mo}_2\text{N}$  phase (carbon supported  $\gamma\text{-Mo}_2\text{N}$  nanoparticles, grain size = 11.2 nm) as shown in Fig. 1c. Interestingly, the  $\text{Mo}_2\text{C}/\text{C}$  catalyst shows an onset potential for the HER similar to that of the  $\text{Mo}_1\text{Soy}$ , however,  $\gamma\text{-Mo}_2\text{N}$  exhibits much lower current densities. Thus, we consider that the high HER activity of the  $\text{Mo}_1\text{Soy}$  catalyst results predominantly from its  $\beta\text{-Mo}_2\text{C}$  phase. We further changed the  $\text{Mo}_1\text{Soy}$  catalyst loading on a specific geometric area in order to study the loading effect of the active  $\text{Mo}_2\text{C}$  phase on the HER activity. Fig. 1d shows the polarization curves of  $\text{Mo}_1\text{Soy}$  catalysts with loading densities of the  $\text{Mo}_2\text{C}$  phase from  $0.35 \text{ mg cm}^{-2}$  up to  $2.8 \text{ mg cm}^{-2}$ . The value of  $\eta_{10}$  for the sample with the  $\text{Mo}_2\text{C}$  loading of  $2.8 \text{ mg cm}^{-2}$  decreases to nearly 150 mV.

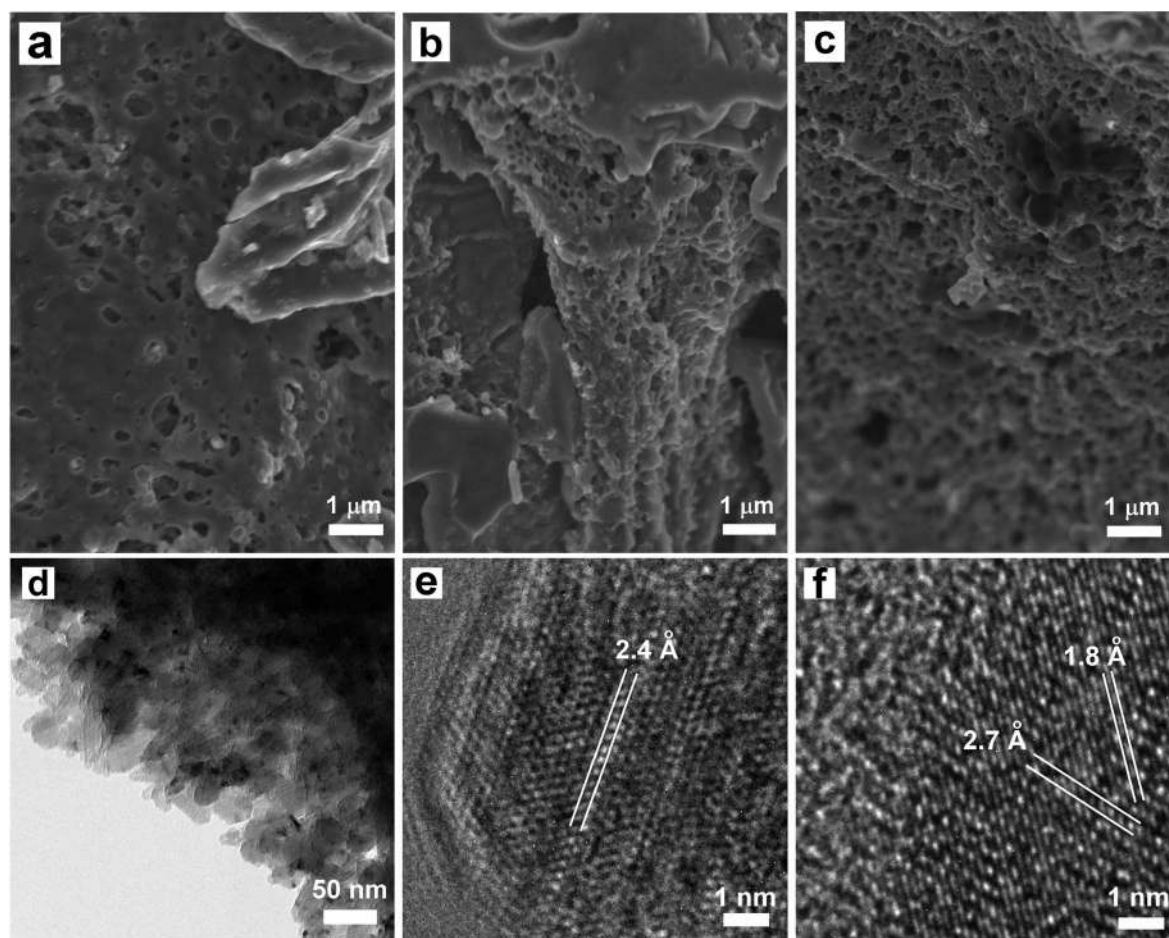


**Fig. 2** Scanning electron micrographs of (a)  $\text{Mo}_{0.1}\text{Soy}$ , (b)  $\text{Mo}_{0.25}\text{Soy}$  and (c)  $\text{Mo}_1\text{Soy}$ . (d) Transmission electron micrograph of the  $\text{Mo}_1\text{Soy}$  catalyst. High resolution TEM images of (e) a  $\gamma\text{-Mo}_2\text{N}$  nanoparticle and (f) a  $\beta\text{-Mo}_2\text{C}$  nanoparticle in the  $\text{Mo}_1\text{Soy}$  catalyst.



### Morphology of the MoSoy catalysts

Scanning electron microscopy (SEM) and transmission electron microscopy (TEM) were used to explore the micro-morphology of the Mo<sub>x</sub>Soy catalysts. The SEM images (Fig. 2a–c) display a morphological transformation from a bulk material with a few pores for the Mo<sub>0.1</sub>Soy to a porous three-dimensional structure with an average pore size of 100 nm for the Mo<sub>1</sub>Soy. However, BET surface area analyses showed that the surface area decreases as *x* increases (Table S1 in the ESI†). This counter-intuitive result arises from the presence of more amorphous carbon in low Mo-loaded samples. The micropores of amorphous carbon contribute significantly to the measured BET surface area. In Fig. 2d, the TEM image shows that the Mo<sub>1</sub>Soy catalyst is assembled from small grains with sizes ranging from 10 to 20 nm. The high-resolution TEM images, as shown in Fig. 2e, reveal the cubic structure of the  $\gamma$ -Mo<sub>2</sub>N nanoparticles with a 2.4 Å spacing of lattice fringes of the {111} planes. From the HRTEM image shown in Fig. 2f, the clearly resolved interplanar distances are measured to be 2.7 and 1.8 Å, corresponding to the {002} and {022} crystal planes of the orthorhombic  $\beta$ -Mo<sub>2</sub>C.

### Electronic states and composition analysis

The charge states and electronic nature of the Mo<sub>1</sub>Soy catalyst were determined by X-ray absorption near-edge structure (XANES) and extended X-ray absorption fine structure (EXAFS) spectroscopies. The Mo K-edge XANES spectra of the Mo precursor, ammonium molybdate (Fig. 3a, orange curve) show

that the pre-edge at 20 004 eV and the edge shifts compared to a Mo foil (grey dashed curve) can be ascribed to the Mo(VI) oxidation state. Mo<sub>2</sub>C/C (green curve) exhibits a higher half-edge energy, which is caused by a negative charge-transfer from molybdenum to carbon.<sup>34</sup> Mo<sub>1</sub>Soy and Mo<sub>2</sub>N/C showed very similar edge energies to that of the Mo foil suggesting that it may be close to a zero-valence state. The details of the Mo binding environment can be described through the *k*<sup>2</sup>-weighted EXAFS Fourier transform magnitudes in *r*-space shown in Fig. 3b. The spectra of the Mo<sub>1</sub>Soy catalyst and Mo<sub>2</sub>C/C are quite similar except for the peaks between *r* = 1 and 2 Å. The EXAFS spectrum of the Mo<sub>1</sub>Soy was fitted with a linear combination of  $\beta$ -Mo<sub>2</sub>C/C and Mo<sub>2</sub>N/C spectra. The best fit is obtained with the ratio of Mo<sub>2</sub>C to Mo<sub>2</sub>N of 0.57 to 0.43 (Fig. 3c, the fit parameters are summarized in Table S2 in the ESI†). This ratio matches very well with that obtained in the aforementioned Rietveld refinement.

Fig. 4 shows the representation of the solid-state reaction we believe to be involved in the formation of the noble-metal-like molybdenum catalysts with soybeans. First, the reactant, ammonium molybdate, undergoes several thermal decomposition steps to give MoO<sub>3</sub>. A previous report<sup>35</sup> has shown that the byproduct, NH<sub>3</sub>, of the thermal decomposition step (130–350 °C) does not react with MoO<sub>3</sub>. A subsequent solid-state reaction between the MoO<sub>3</sub> and the amino groups on soybean proteins leads to the formation of  $\gamma$ -Mo<sub>2</sub>N,<sup>36,37</sup> and elemental carbon transforms molybdenum into stable  $\beta$ -Mo<sub>2</sub>C.<sup>38</sup> The EDX spectra of the Mo<sub>1</sub>Soy sample (Fig. S4 in the ESI†) showed the presence of a trace amount of potassium (atomic ratio of K/Mo = 0.103). HER

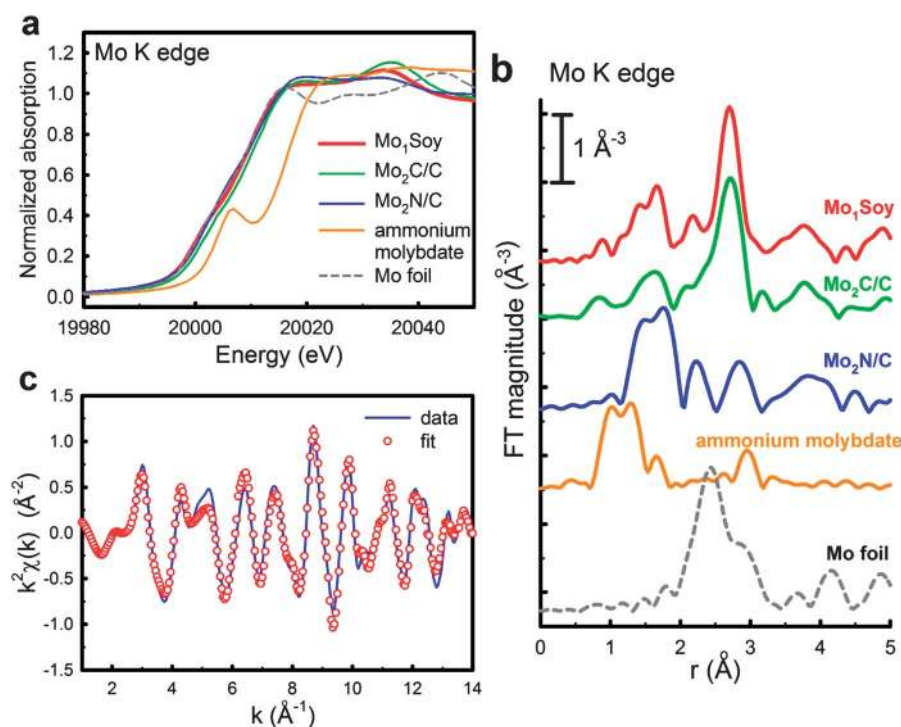


**Fig. 3** (a) XANES spectra and (b) *k*<sup>2</sup>-weighted EXAFS Fourier transform magnitudes of the Mo K-edge from the Mo<sub>1</sub>Soy catalyst, the Mo<sub>2</sub>C/C, the Mo<sub>2</sub>N/C nanoparticles, and raw ammonium molybdate as well as a Mo foil. (c) *k*<sup>2</sup>-weighted EXAFS spectra and the linear combination fitting calculated from the spectra of Mo<sub>2</sub>N/C and Mo<sub>2</sub>C/C.

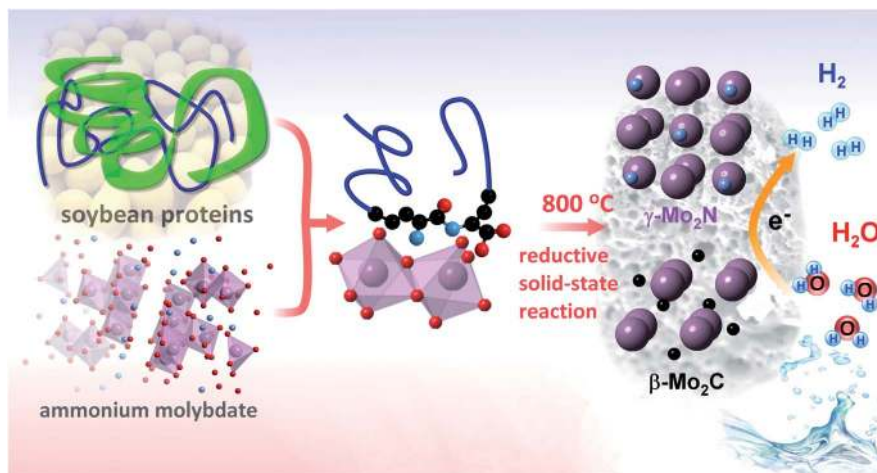


**Fig. 4** The synthesis from soybeans and ammonium molybdate of a solid catalyst suitable for electrochemical hydrogen production. A solid-state reaction between soybeans and the molybdate leads to their reductive carbonization and nitridation, so as to form  $\beta$ - $\text{Mo}_2\text{C}$  and  $\gamma$ - $\text{Mo}_2\text{N}$  crystals. The structure of the amino moieties (blue balls) of soybean proteins is indicated. Plum balls: Mo, blue balls: N, black balls: C, and red balls: oxygen.

analyses of the  $\text{Mo}_2\text{N}$ - $\text{Mo}_2\text{C}$  mixture and the K-added  $\text{Mo}_2\text{N}$ - $\text{Mo}_2\text{C}$  mixture (Fig. S5 in the ESI†) demonstrated that (1) the physical mixture of  $\text{Mo}_2\text{N}/\text{C}$  and  $\text{Mo}_2\text{C}/\text{C}$  does not perform as well as the  $\text{Mo}_1\text{Soy}$  catalyst and (2) the presence of potassium in the  $\text{Mo}_2\text{N}$ - $\text{Mo}_2\text{C}$  hybrid does not affect its HER activity. Therefore, we attribute  $\text{Mo}_1\text{Soy}$ 's high activity to the synergistic effect between the  $\beta$ - $\text{Mo}_2\text{C}$  phase and the  $\gamma$ - $\text{Mo}_2\text{N}$  phase in the composite material; the presence of nitrogen and carbon atoms in the vicinity of the catalytic molybdenum center facilitates the production of hydrogen from water.

#### Anchoring MoSoy on graphene sheets

Very recently graphene sheets have been found to be an excellent support for HER catalysts by Dai's group.<sup>39</sup> In the present study, the  $\text{Mo}_1\text{Soy}$  composition has been supported on reduced graphene oxide (RGO) sheets. The sponge-like structure is no longer observed on the resulting  $\text{Mo}_1\text{Soy}$ -RGO composite (Fig. S6 in the ESI†). Instead, the RGO sheets are uniformly

decorated with  $\text{Mo}_2\text{C}$ - $\text{Mo}_2\text{N}$  composite nanoparticles as shown in Fig. 5a. The superimposed crystalline stripes shown in the inset of Fig. 5a indicate that the small  $\text{Mo}_2\text{C}$  and  $\text{Mo}_2\text{N}$  nanocrystals, with sizes from 1 to 7 nm, agglomerate or lay over each other. The polarization curve of the  $\text{Mo}_1\text{Soy}$ -RGO catalyst in Fig. 5b shows a further improvement in the HER activity even though the  $\text{Mo}_2\text{C}$  loading of the  $\text{Mo}_1\text{Soy}$ -RGO composite ( $0.47 \text{ mg cm}^{-2}$ ) is only one third of that of the pristine  $\text{Mo}_1\text{Soy}$  catalyst ( $1.4 \text{ mg cm}^{-2}$ ). The HER performance of  $\text{Mo}_1\text{Soy}$ -RGO exhibits a  $\eta_{10}$  of 109 mV, a performance that exceeds that of the bulk Pt electrode and is only 48 mV larger than that of the commercial Pt/C catalyst. Its Faradaic yield was found to be nearly 99.99% as described in Fig. S7 of the ESI.† Furthermore, the high mass activity of  $\text{Mo}_1\text{Soy}$ -RGO distinguishes it from the other non-noble-metal HER catalysts (Table S3 in the ESI†). These results imply that faster electron transfer occurs on the RGO-supported  $\text{Mo}_1\text{Soy}$  catalyst. This was further examined using electrochemical impedance spectroscopy (EIS) analyses.

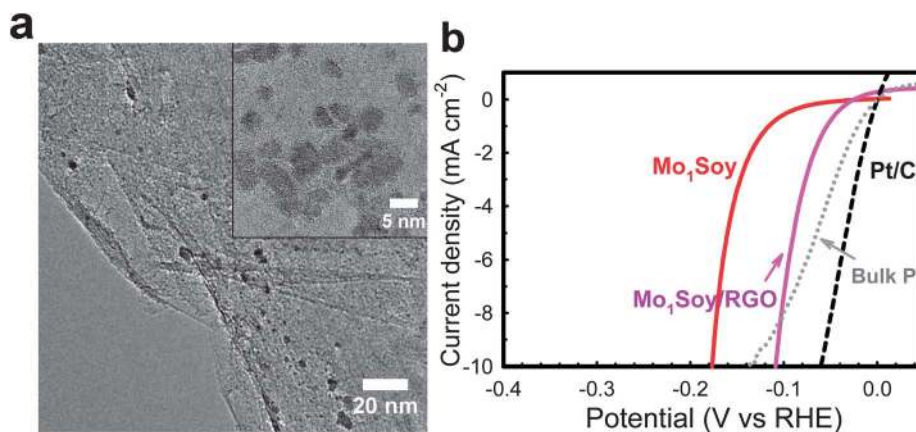


**Fig. 5** (a) The TEM micrographs of the RGO-supported  $\text{Mo}_1\text{Soy}$  catalyst. The inset picture is a HRTEM image with a magnification of 500 000 showing that the size of nanocatalysts ranged from 1 to 7 nm. (b) The polarization curve of RGO-supported  $\text{Mo}_1\text{Soy}$  catalyst (loading:  $0.47 \text{ mg Mo}_2\text{C cm}^{-2}$ ) showing further improvement of the HER activity.

### Electrochemical impedance spectroscopy analysis

The resulting Nyquist plot of the Mo<sub>1</sub>Soy-RGO catalyst at overpotentials from 0 to 200 mV (Fig. 6a) exhibited classical two-time-constant behavior. A good approximation to the experimental data was obtained using the two-time-constant model (see Fig. S8 in the ESI†). In Fig. 6a, the charge-transfer resistance,  $R_{ct}$ , determined from the semicircle registered at low frequencies (high  $Z'$ ), is found to be overpotential-dependent. The Nyquist profiles collected at  $\eta = 100$  mV on the Mo<sub>1</sub>Soy and Mo<sub>1</sub>Soy-RGO electrodes are compared in Fig. 6b. The Mo<sub>1</sub>Soy-RGO catalyst exhibited lower charge-transfer impedance ( $9\ \Omega$ ) than did the Mo<sub>1</sub>Soy electrode ( $31.7\ \Omega$ ), and a much lower charge-transfer impedance than the Mo<sub>2</sub>C/C ( $36.1\ \Omega$ ) and bulk Mo<sub>2</sub>C ( $1600\ \Omega$ ) as presented in Table S4 in the ESI†. This result suggests that the combination of a RGO support and the Mo<sub>1</sub>Soy catalyst affords faster electron transport from the Mo<sub>2</sub>C active sites to protons. Under comparable conditions, the RGO-supported MoS<sub>2</sub> catalyst was reported to exhibit a charge transfer impedance of  $250\ \Omega$  at an overpotential of 120 mV.<sup>39</sup> Therefore, the high rate of the electron transfer reaction on the Mo<sub>1</sub>Soy-RGO catalyst is particularly noteworthy.

The classic two-electron-reaction models for the cathodic hydrogen evolution in acidic and aqueous media reveal that the HER proceeds in two steps: hydrogen adsorption and subsequent desorption to form molecular hydrogen. It is then obvious from

the presented EIS analysis that the overall rate of the HER is related to the charge transfer resistance. The dependence of the obtained impedance on the applied potential has been shown to correspond to the Tafel slope of the proton discharging step.<sup>40</sup> In Fig. 6c, the potential is plotted *versus* the inverse  $R_{ct}$  on a logarithmic scale for various catalysts considered in this work, yielding a linear dependence for each of them. For bulk Mo<sub>2</sub>C, the slope ( $b_R$ ) of 87.6 mV per decade (Table S4†) obtained from the linear fit suggests that hydrogen evolution occurs *via* a Volmer–Heyrovský mechanism in which the Volmer reaction is the rate-limiting step. For the Mo<sub>1</sub>Soy and Mo<sub>1</sub>Soy-RGO catalysts, the smaller slopes of 66.4 and 62.7 mV per decade, respectively, suggest faster proton discharge kinetics than that with bulk Mo<sub>2</sub>C. In the charge-transfer-limited region (small overpotentials), the exchange current density,  $j_{0,R}$ , can be determined by the charge-transfer resistance (Table S4†). The Mo<sub>1</sub>Soy-RGO composite exhibited high  $j_{0,R}$  ( $3.7 \times 10^{-2}\ \text{mA cm}^{-2}$ ) which is 54 times higher than that of bulk Mo<sub>2</sub>C, and 2.8 times higher than the Mo<sub>1</sub>Soy catalyst. The direct growth of anchored nanocrystals on RGO may afford the formation of strongly coupled hybrid materials with intimate, seamless electron transfer pathways. Theoretical studies have shown that the strong hybridization of the metal's d-orbital and the  $\pi$ -orbital of the underlying graphene sheets expands the density of states of the metal d-orbitals.<sup>41</sup> RGO-supported nanocrystals have exhibited either an enhanced

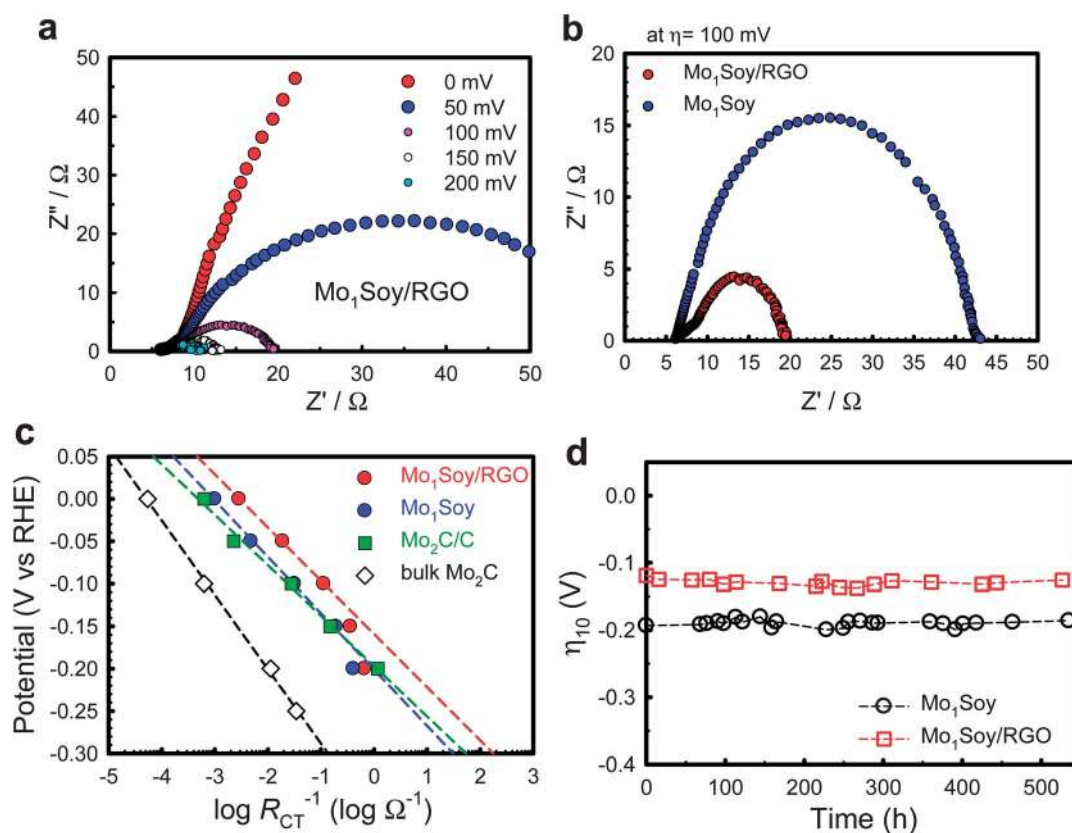


**Fig. 6** (a) Nyquist plots of the Mo<sub>1</sub>Soy-RGO catalyst recorded at selected overpotentials in a H<sub>2</sub>-purged 0.1 M HClO<sub>4</sub> solution. (b) Comparison of the Nyquist plots of the Mo<sub>1</sub>Soy and Mo<sub>1</sub>Soy-RGO catalysts collected at  $\eta = 100$  mV. (c) Semi-logarithmic plot of applied potential vs.  $\log(R_{ct}^{-1})$ . (d) Long-term durability tests of the Mo<sub>1</sub>Soy (loading: 1.18 mg cm<sup>-2</sup> Mo<sub>2</sub>C) and Mo<sub>1</sub>Soy-RGO catalysts (loading: 0.47 mg cm<sup>-2</sup> Mo<sub>2</sub>C).



charge-transfer rate, high capacitance, or improved catalytic activity in electrochemical devices such as batteries, supercapacitors, fuel cells and water electrolyzers.<sup>42</sup> We envisage that anchoring Mo<sub>1</sub>Soy nanocrystals on RGO sheets induces a strong coupling of the Mo center with the  $\pi$ -electrons of the underlying graphene sheet, thus accelerating the electron transfer rate for the chemical desorption of H<sub>ads</sub> and H<sup>+</sup> and further reducing the input overpotential. Further studies are being pursued to gain a deeper understanding of the nature of the catalyst–RGO interface interaction.

### Durability

The most critical problem in hydrogen production using non-noble-metal catalysts is the deterioration of activity in acidic environments owing to their poor corrosion stability. To determine whether the Mo<sub>1</sub>Soy catalysts meet this essential corrosion stability requirement, we carried out a long-term test in a 0.1 M HClO<sub>4</sub> solution. Fig. 6d depicts the overpotential recorded for driving the HER at  $j = 10 \text{ mA cm}^{-2}$  as a function of time. The test was paused occasionally for refreshing the electrolyte. The overpotential for both the Mo<sub>1</sub>Soy and Mo<sub>1</sub>Soy–RGO catalysts remained almost the same over 500 hours of operation. An accelerated deterioration experiment was carried out on the  $\beta$ -Mo<sub>2</sub>C/C,  $\gamma$ -Mo<sub>2</sub>N/C, Mo<sub>1</sub>Soy and the Mo<sub>1</sub>SoyRGO catalysts. In this test, potential sweeps were applied from  $-0.3$  to  $+0.63 \text{ V}$  at  $100 \text{ mV s}^{-1}$  in 0.1 M HClO<sub>4</sub> solutions for 3000 cycles, and then a polarization curve was recorded at  $2 \text{ mV s}^{-1}$  in a fresh 0.1 M HClO<sub>4</sub> solution. After 3000 cycles, the Mo<sub>1</sub>Soy, the Mo<sub>1</sub>Soy–RGO and the  $\gamma$ -Mo<sub>2</sub>N/C catalysts retained polarization curves nearly identical to those before potential cycling (Fig. S9a in the ESI†). The  $\eta_{10}$  value (Table S4†) merely changed by 8 and 7 mV after 3000 cycles for the Mo<sub>1</sub>Soy–RGO and Mo<sub>1</sub>Soy electrodes, respectively, indicating that degradation hardly occurred. The same test on the  $\beta$ -Mo<sub>2</sub>C/C sample showed significant degradation of the activity (Fig. S9b†), and its  $\eta_{10}$  increased by more than 100 mV. These results afford evidence that a synergy between the  $\gamma$ -Mo<sub>2</sub>N and  $\beta$ -Mo<sub>2</sub>C phases exerts a stabilizing effect on the MoSoy catalysts against acids, and thus enhances the long-term durability.

### Conclusions

Non-precious-metal-based catalysts have typically shown much lower activities for hydrogen production than Pt-based catalysts in acidic media.<sup>43</sup> The molybdenum catalyst reported in the present work takes advantage of porous three-dimensional structure and ligand-modified catalytic properties to achieve an efficient and stable HER activity rivaling that of Pt catalysts under realistic conditions. This study unambiguously provides evidence that a cheap and earth-abundant transition metal such as molybdenum can be turned into an active catalyst by the controlled solid-state reaction with soybeans. The RGO-supported MoSoy catalyst produced hydrogen fuel at remarkably low overpotentials. Most importantly, the preparation of the MoSoy catalyst is simple and can be easily scaled up. Its long-term durability and ultra-low capital cost satisfy the

prerequisites for its application in the construction of large-scale devices. These findings thus open up new prospects for combining inexpensive biomass and transition metals such as W, Nb, Ta and V to produce catalysts for electrocatalytic reactions. Further improvements in the HER activity of this catalyst could potentially be achieved by incorporating promoter elements such as Cu, Co, Ni and Fe, which have been found to enhance the activity of molybdenum sulfides.

## Materials and methods

### Material synthesis

The solid-state reaction of soybeans (organic yellow dry soybeans supplied by the Whole Food Market, Inc.) with ammonium molybdate ((NH<sub>4</sub>)<sub>6</sub>Mo<sub>7</sub>O<sub>24</sub>·4H<sub>2</sub>O, Aldrich) is capable of producing catalysts that convert water into hydrogen fuel through electrolysis. The typical procedure for preparing the catalyst is as follows. The dry soybeans were ground into a powder. A mixture of ammonium molybdate and the soybean powder was dispersed in water and sonicated for 30 min. The mixture was dried in an oven at 80 °C for 6 h. The dried powder was then placed in a quartz boat and calcined at 800 °C under Ar in a quartz tube furnace for 2 h. This procedure yielded a dark-grey powder (Mo<sub>x</sub>Soy,  $x$  is the weight ratio (g/g) of ammonium molybdate to soybean powder) which was ground again to make a fine powder. The weight ratio ( $x$ ) tested includes 0.1, 0.25 and 1.0. The RGO-supported MoSoy was synthesized using a similar procedure, except that RGO was added to the solution mixture of soybean powder and ammonium molybdate.

Vulcan XC-72R carbon black-supported molybdenum carbide (Mo<sub>2</sub>C/C, grain size = 11.2 nm) was prepared by carburization of carbon-supported ammonium molybdate ((NH<sub>4</sub>)<sub>6</sub>Mo<sub>7</sub>O<sub>24</sub>·4H<sub>2</sub>O, Aldrich) in a tube furnace purged with an Ar flow at 800 °C for 2 h according to the procedure given in a previous report.<sup>34</sup> The carbon black-supported molybdenum nitride (Mo<sub>2</sub>N/C, grain size = 8.5 nm) was prepared by annealing a mixture of MoO<sub>3</sub> powder and the Vulcan XC-72R carbon black in a NH<sub>3</sub>-purged tube furnace at 700 °C for 2 h. The grain sizes of Mo<sub>2</sub>C and Mo<sub>2</sub>N were estimated from XRD signals.

### Electrochemical measurements

The electrodes for the electrochemical measurements were fabricated as follows. Catalyst ink was prepared by mixing Mo<sub>x</sub>Soy catalyst powder with a 20% Nafion dispersion (DuPont) (100 mg of solid Nafion for 100 mg of catalyst) into a slurry. The catalyst–Nafion slurry was loaded into a 1 cm<sup>2</sup> surface area on a strip of 1 × 2 cm<sup>2</sup> carbon paper (Toray TGP-H-060 carbon paper). The electrode was then dried under vacuum. The 0.1 M HClO<sub>4</sub>(aq) electrolytes for electrochemical measurements were prepared from Optima perchloric acid obtained from Fisher and Milli-Q UV-plus water (Millipore). A commercial Pt/C (10 wt %) electrode from E-TEK was used as received. The electrochemical measurements were carried out in a typical two-chamber, three-electrode cell. An Ag/AgCl/KCl (3 M) electrode was used with a double-junction chamber as a reference. All potentials are quoted with respect to reversible hydrogen

electrode (RHE) and are ohmic resistance-corrected. The polarization curves for the hydrogen evolution reaction were described using the equation,  $\eta = a + b \ln j + jR_s$ , where  $\eta$  (V) denotes the applied overpotential,  $j$  (mA cm<sup>-2</sup>) the current density,  $b$  (V per decade) the Tafel slope, and  $R_s$  ( $\Omega$  cm<sup>2</sup>) the total area-specific uncompensated resistance of the system which was estimated from the high-frequency impedance in the Nyquist plots of electrochemical impedance spectroscopy analyses. Thus, the experimental overpotential can be corrected by subtracting the ohmic drop according to the equation:  $\eta_{\text{corr}} = \eta - jR_s$ . A Pt foil was used as the auxiliary electrode. The working electrode and the auxiliary electrode were separated by a glass frit. All voltammetry experiments were carried out using a BASi Epsilon electrochemical workstation at room temperature.

Polarization curves were collected in a H<sub>2</sub>-purged 0.1 M HClO<sub>4</sub> solution at a scan rate of 2 mV s<sup>-1</sup>. The long-term durability tests were performed in an Ar-purged 0.1 M HClO<sub>4</sub> solution by recording the overpotential needed to drive 10 mA cm<sup>-2</sup> of current density.

The EIS measurements were carried out on a CHI 6044d potentiostat from 100 000 Hz to 0.01 Hz at selected values of the overpotential ( $\eta = 0$  to 250 mV) with an amplitude of 5 mV.

### Thermogravimetric/differential thermal analysis (TG/DTA)

Thermogravimetric measurements and differential thermal analysis were performed with a Perkin Elmer Diamond thermogravimetric/differential thermal analyzer. The sample was placed in an alumina sample holder. Measurements in pure argon with a flow rate of 100 ml min<sup>-1</sup> were carried out over a temperature range of 50–800 °C at a heating rate of 20 °C min<sup>-1</sup> and then held at 800 °C for 2 h.

### Electron microscopy

Scanning electron micrographs were collected on a JEOL SEM 7600F. High-resolution transmission electron microscopy (TEM) imaging was performed using a JEOL JEM3000F TEM equipped with a field emission gun and a Gatan imaging filter (GIF). The instrument was operated at 300 kV.

### Powder X-ray diffraction spectroscopy

Measurements were taken with a Rigaku Miniflex II diffractometer using Cu K $\alpha$  radiation ( $\lambda = 1.54056$  Å). The patterns were collected from 10 to 80° at a scanning rate of 0.25° min<sup>-1</sup>, with a step size of 0.01°. The grain sizes were calculated using the Debye–Scherer equation,

$$D_{hkl} = \frac{k_{hkl}\lambda}{\beta_{hkl} \cos(\theta)}$$

where  $\lambda$  is the wavelength of the X-rays ( $\lambda = 1.54$  Å) and  $\beta_{hkl}$  (or FWHM) is the angular line width. The peak at  $2\theta = 39.5^\circ$  in the XRD spectra of  $\beta$ -Mo<sub>2</sub>C is composed of the (2 1 1) peak at  $2\theta = 39.468^\circ$  and the (0 1 2) peak at  $2\theta = 39.560^\circ$ . The two peaks contribute equally to the 39.5° signal. Thus the grain size of  $\beta$ -Mo<sub>2</sub>C was calculated based on the full width at quarter maximum of the 39.5° signal. The size of  $\gamma$ -Mo<sub>2</sub>N crystals was based on its (111) lattice plane.

The Rietveld profile refinements were performed with the aid of GSAS software. The series of powder patterns was refined by sequential analysis wherein the starting model was based on the earlier powder pattern.

### Synchrotron X-ray absorption spectroscopy

The X-ray absorption spectroscopy (XAS) measurements were undertaken at the National Synchrotron Light Source (NSLS), BNL at the X18B beamline. The measurements were carried out at the Mo K-edge (20 000 eV) at room temperature. The XAS data were acquired in both the transmission and fluorescence modes, although the data presented in this report were obtained in the former. The data acquired were processed and analyzed by Athena and Artemis software.

## Acknowledgements

The authors thank Dr Chun-Han Hsu at National Cheng Kung University for surface area analysis and Enyuan Hu at Stony Brook University for Rietveld refinement. This work was carried out at Brookhaven National Laboratory (BNL) under contract DE-AC02-98CH10886 with the U. S. Department of Energy (DOE) and supported by its Division of Chemical Sciences, Geosciences and Biosciences, Office of Basic Energy Sciences. Initial stages of this work were supported by BNL Laboratory Directed Research and Development (LDRD) Project no. 10-015. C.H.W. and K.S. acknowledge support by BNL Technology Maturation Funding TM12-008. Shilpa I. and Shweta I. gratefully acknowledge support by the BNL Office of Educational Programs. Beamline X18B at the NSLS is supported in part by the Synchrotron Catalysis Consortium, U. S. Department of Energy Grant no. DE-FG02-05ER15688. XRD and SEM were carried out at the Center for Functional Nanomaterials.

## Notes and references

- 1 Hydrogen production road map: Technology pathways to the future, FreedomCAR & Fuel partnership. Hydrogen Production Technical Team, 2009.
- 2 J. A. Turner, *Science*, 2004, **305**, 972–974.
- 3 N. S. Lewis and D. G. Nocera, *Proc. Natl. Acad. Sci. U. S. A.*, 2006, **103**, 15729–15735.
- 4 M. G. Walter, E. L. Warren, J. R. McKone, S. W. Boettcher, Q. X. Mi, E. A. Santori and N. S. Lewis, *Chem. Rev.*, 2010, **110**, 6446–6473.
- 5 J. Turner, G. Sverdrup, M. K. Mann, P.-C. Maness, B. Kroposki, M. Ghirardi, R. J. Evans and D. Blake, *Int. J. Energy Res.*, 2008, **32**, 379–407.
- 6 K. Ayers, *DOE Annual Merit Review Proceedings, Hydrogen and Fuel Cells Program*, Arlington Virginia, 2012.
- 7 D. V. Esposito, S. T. Hunt, Y. C. Kimmel and J. G. Chen, *J. Am. Chem. Soc.*, 2012, **134**, 3025–3033.
- 8 X. Wang, K. Maeda, A. Thomas, K. Takanabe, G. Xin, J. M. Carlsson, K. Domen and M. Antonietti, *Nat. Mater.*, 2009, **8**, 76–80.



- 9 S. Cobo, J. Heidkamp, P. A. Jacques, J. Fize, V. Fourmond, L. Guetaz, B. Jousselmé, V. Ivanova, H. Dau, S. Palacin, M. Fontecave and V. Artero, *Nat. Mater.*, 2012, **11**, 802–807.
- 10 M. L. Helm, M. P. Stewart, M. Bullock, M. R. DuBois and D. L. DuBois, *Science*, 2011, **333**, 863–866.
- 11 J. G. Highfield, E. Claude and K. Oguro, *Electrochim. Acta*, 1999, **44**, 2805–2814.
- 12 J. R. McKone, E. L. Warren, M. J. Bierman, S. W. Boettcher, B. S. Brunschwig, N. S. Lewis and H. B. Gray, *Energy Environ. Sci.*, 2011, **4**, 3573–3583.
- 13 E. L. Warren, J. R. McKone, H. A. Atwater, H. B. Gray and N. S. Lewis, *Energy Environ. Sci.*, 2012, **5**, 9653–9661.
- 14 L. Birry and A. Lasia, *J. Appl. Electrochem.*, 2004, **34**, 735–749.
- 15 T. F. Jaramillo, J. Bonde, J. D. Zhang, B. L. Ooi, K. Andersson, J. Ulstrup and I. Chorkendorff, *J. Phys. Chem. C*, 2008, **112**, 17492–17498.
- 16 T. F. Jaramillo, K. P. Jørgensen, J. Bonde, J. H. Nielsen, S. Hørch and I. Chorkendorff, *Science*, 2007, **317**, 100–102.
- 17 S. Wirth, F. Harnisch, M. Weinmann and U. Schröder, *Appl. Catal., B*, 2012, **126**, 225–230.
- 18 F. Harnisch, G. Sievers and U. Schröder, *Appl. Catal., B*, 2009, **89**, 455–458.
- 19 H. I. Karunadasa, E. Montalvo, Y. Sun, M. Majda, J. R. Long and C. J. Chang, *Science*, 2012, **335**, 698–702.
- 20 Y. Sun, H. Cheng, S. Gao, Z. Sun, Q. Liu, Q. Liu, F. Lei, T. Yao, J. He, S. Wei and Y. Xie, *Angew. Chem. Int. Ed.*, 2012, **51**, 8727–8731.
- 21 W.-F. Chen, K. Sasaki, C. Ma, A. I. Frenkel, N. Marinkovic, J. T. Muckerman, Y. Zhu and R. R. Adzic, *Angew. Chem. Int. Ed.*, 2012, **51**, 6131–6135.
- 22 Z. Z. Wu, B. Z. Fang, A. Bonakdarpour, A. K. Sun, D. P. Wilkinson and D. Z. Wang, *Appl. Catal., B*, 2012, **125**, 59–66.
- 23 P. D. Tran, M. Nguyen, S. S. Pramana, A. Bhattacharjee, S. Y. Chiam, J. Fize, M. J. Field, V. Artero, L. H. Wong, J. Loo and J. Barber, *Energy Environ. Sci.*, 2012, **5**, 8912–8916.
- 24 P. D. Tran, S. S. Pramana, V. S. Kale, M. Nguyen, S. Y. Chiam, S. K. Batabyal, L. H. Wong, J. Barber and J. Loo, *Chem.–Eur. J.*, 2012, **18**, 13994–13999.
- 25 B. Seger, A. B. Laursen, P. C. K. Vesborg, T. Pedersen, O. Hansen, S. Dahl and I. Chorkendorff, *Angew. Chem. Int. Ed.*, 2012, **51**, 9128–9131.
- 26 D. Merki, S. Fierro, H. Vrubel and X. L. Hu, *Chem. Sci.*, 2011, **2**, 1262–1267.
- 27 H. Vrubel, D. Merki and X. Hu, *Energy Environ. Sci.*, 2012, **5**, 6136–6144.
- 28 D. Merki, H. Vrubel, L. Rovelli, S. Fierro and X. L. Hu, *Chem. Sci.*, 2012, **3**, 2515–2525.
- 29 D. Merki and X. L. Hu, *Energy Environ. Sci.*, 2011, **4**, 3878–3888.
- 30 Z. Chen, D. Cummins, B. N. Reinecke, E. Clark, M. K. Sunkara and T. F. Jaramillo, *Nano Lett.*, 2011, **11**, 4168–4175.
- 31 J. Kibsgaard, Z. B. Chen, B. N. Reinecke and T. F. Jaramillo, *Nat. Mater.*, 2012, **11**, 963–969.
- 32 J. D. Benck, Z. B. Chen, L. Y. Kuritzky, A. J. Forman and T. F. Jaramillo, *ACS Catal.*, 2012, **2**, 1916–1923.
- 33 H. Vrubel and X. Hu, *Angew. Chem. Int. Ed.*, 2012, **51**, 12703–12706.
- 34 W.-F. Chen, C. H. Wang, K. Sasaki, N. Marinkovic, W. Xu, J. T. Muckerman, Y. Zhu and R. R. Adzic, *Energy Environ. Sci.*, 2013, **6**, 943–951.
- 35 Z. L. Yin, X. H. Li, G. Z. Zhou, Q. S. Zhao and S. Y. Chen, *Trans. Nonferrous Met. Soc. China*, 1996, **6**, 26–28.
- 36 H.-M. Wang, X.-H. Wang, M.-H. Zhang, X.-Y. Du, W. Li and K.-Y. Tao, *Chem. Mater.*, 2007, **19**, 1801–1807.
- 37 P. Afanasiev, *Inorg. Chem.*, 2002, **41**, 5317–5319.
- 38 E. L. Kugler, C. H. Clark, J. H. Wright, D. B. Dadyburjor, J. C. Hanson, Z. Song, T. Cai and J. Hrbek, *Top. Catal.*, 2006, **39**, 257–262.
- 39 Y. Li, H. Wang, L. Xie, Y. Liang, G. Hong and H. Dai, *J. Am. Chem. Soc.*, 2011, **133**, 7296–7299.
- 40 E. Navarro-Flores, Z. Chong and S. Omanovic, *J. Mol. Catal. A: Chem.*, 2005, **226**, 179–197.
- 41 C. Gong, G. Lee, B. Shan, E. M. Vogel, R. M. Wallace and K. Cho, *J. Appl. Phys.*, 2010, **108**, 123711.
- 42 Y. Liang, Y. Li, H. Wang and H. Dai, *J. Am. Chem. Soc.*, 2013, **135**, 2013–2036.
- 43 T. R. Cook, D. K. Dogutan, S. Y. Reece, Y. Surendranath, T. S. Teets and D. G. Nocera, *Chem. Rev.*, 2010, **110**, 6474–6502.